Compensation between Resolved and Unresolved Wave Driving in the Stratosphere: Implications for Downward Control

NAFTALI Y. COHEN, EDWIN P. GERBER, AND OLIVER BÜHLER

Center for Atmosphere Ocean Science, Courant Institute of Mathematical Sciences, New York University, New York, New York

(Manuscript received 17 December 2012, in final form 3 June 2013)

ABSTRACT

Perturbations to the orographic gravity wave parameterization scheme in an idealized general circulation model reveal a remarkable degree of compensation between the parameterized and the resolved wave driving: when the orographic gravity wave driving is changed, the resolved wave driving tends to change in the opposite direction, so there is little impact on the Brewer–Dobson circulation. Building upon earlier observations of such compensation, an analysis based on quasigeostrophic theory suggests that the compensation between the resolved and parameterized waves is inevitable when the stratosphere is driven toward instability by the parameterized gravity wave driving. This instability, however, is quite likely for perturbations of small meridional length scale in comparison with the Rossby radius of deformation. The insight from quasigeostrophic theory is confirmed in a systematic study with an idealized general circulation model and supported by analyses of comprehensive models. The compensation between resolved and unresolved waves suggests that the commonly used linear separation of the Brewer–Dobson circulation into components (i.e., resolved versus parameterized wave driving) may provide a potentially misleading interpretation of the role of different waves. It may also, in part, explain why comprehensive models tend to agree more on the total strength of the Brewer–Dobson circulation than on the flow associated with individual components. This is of particular relevance to diagnosed changes in the Brewer–Dobson circulation in climate scenario integrations as well.

1. Introduction

The Brewer–Dobson circulation (BDC), first hypothesized by Dobson et al. (1929) and established by Brewer (1949), is a wave-driven zonal-mean mass transport circulation in the stratosphere, with air parcels ascending from the tropical troposphere to the extratropical stratosphere and descending in the middle and high latitudes (e.g., Holton et al. 1995). The importance of the BDC lies in the fact that, together with stratospheric chemistry, it sets the distribution of stratospheric ozone and water vapor. Stratospheric ozone is of great importance as it absorbs the sun's harmful shortwave radiation and serves as a greenhouse gas that absorbs longwave radiation from the ground, and thus is an important factor in the atmosphere's radiation budget (e.g., Haynes 2005). In addition, recent studies show evidence that Southern Hemisphere tropospheric circulation trends are strongly influenced by stratospheric ozone concentration changes (e.g., Thompson and Solomon 2002; Son et al. 2010), and Solomon et al. (2010) find that stratospheric water vapor concentration is an important driver of decadal global surface climate change.

The current physical interpretation of the extratropical BDC was developed in the 1960s and 1970s [see Haynes (2005) for an overview] and is usually expressed in terms of the transformed Eulerian-mean (TEM) equations. The strength of the TEM equations comes from the fact that its meridional and vertical velocities approximate the Lagrangian-mean velocities for zonal-mean steady disturbances (e.g., Bühler 2009, chapter 11). Moreover, in the quasigeostrophic (QG) approximation the TEM equations provide a clear causality of the wave–mean flow driving, a point that is emphasized in the ''downward control'' principle (Haynes et al. 1991).

Planetary-scale Rossby waves and small-scale gravity waves are the primary drivers of the circulation in the middle atmosphere, where planetary waves dominate in the stratosphere and gravity waves dominate in the mesosphere. Stationary Rossby waves are forced by large-scale

Corresponding author address: Naftali Cohen, Courant Institute of Mathematical Sciences, 251 Mercer St., New York, NY 10012. E-mail: naftali@cims.nyu.edu

DOI: 10.1175/JAS-D-12-0346.1

mountains and land–sea contrast, and so resolved in atmospheric general circulation models (AGCMs), whereas gravity waves that originate from small-scale mountains, convection, and frontal instabilities cannot be captured in most of the AGCMs and so need to be parameterized (Fritts and Alexander 2003; Alexander et al. 2010).

A key aim of this study is to provide a better understanding of how waves of different scales contribute to the BDC. The common practice today (e.g., Butchart et al. 2011) is to use the downward control principle to linearly separate the influence of resolved planetary-scale Rossby wave driving [the Eliassen–Palm flux divergence (EPFD)] and parameterized orographic and nonorographic gravity wave driving (OGW and NOGW, respectively; an extra ''D'' is added, from time to time, to denote ''driving''). Denoting the zonal-mean wave driving by $\overline{G}$, then $\overline{G}_{\rm Tot} = \overline{G}_{\rm EPFD} + \overline{G}_{\rm OGW} + \overline{G}_{\rm NOGW}$: the total wave driving is the sum of contributions from the resolved Rossby wave driving and the unresolved parameterized orographic and nonorographic gravity wave driving. The downward control principle relates a unique (up to a boundary condition) residual-mean meridional circulation $\overline{\psi}^*$ to the total wave driving. It is then argued that the total residual-mean meridional circulation can be viewed as a linear sum of the residual-mean meridional circulation driven by the different waves. Hence, $\overline{\psi}^*_{\rm Tot} = \overline{\psi}^*_{\rm EPFD} + \overline{\psi}^*_{\rm OGW} + \overline{\psi}^*_{\rm NOGW}$; each component is associated with the respective wave driving contribution. Under this assumption, it is found that at 70 hPa, the resolved waves, OGW and NOGW, contribute roughly 70%, 20%, and 10% of the BDC, respectively (Butchart et al. 2011). However, there is a wide spread between the models in the contributions from the different types of waves. For example, different stratosphere resolving models from the Chemistry Climate Model Validation Activity, phase 2 (CCMVal2), suggest that the contributions from resolved waves, OGW, and NOGW ranged roughly from 30% to 100%, 0% to 40%, and 0% to 20%, respectively (Butchart et al. 2011).

Climate change studies with chemistry–climate models consistently predict a strengthening of about 2% decade^{-1} in the BDC throughout the twenty-first century (Butchart et al. 2006, 2010; Eyring et al. 2010). Overall, the downward control decomposition suggests that at 70 hPa, resolved wave and parameterized gravity wave driving account for roughly two-thirds and one-third of the trend, respectively. There is considerable disagreement between models, however; in some models the parameterized OGW even dominate the trend (e.g., Garcia and Randel 2008; Li et al. 2008; McLandress and Shepherd 2009; Eyring et al. 2010).

This linear decomposition of the forcing gives the impression that each component of the system is responsible for driving a fraction of the total circulation. Thus, for example, if models are overestimating changes in gravity wave driving, should one think they are overestimating the total trend in the BDC? An earlier study of interactions between orographic gravity wave drag and resolved waves by McLandress and McFarlane (1993) suggests that one should be cautious in drawing such a conclusion. They found that OGW torque in the mesosphere can generate planetary-scale waves, leading to a nearly equal and opposite resolved wave torque. While they study in depth the quasi-linear structure of these interactions, here we concentrate on their zonal-mean structure, which is relevant to the Brewer–Dobson circulation. We show that there may be substantial interactions between resolved and parameterized waves throughout the stratosphere: if one component of the system is altered, the others may act to compensate for the change. Hence, the decomposition of the BDC into individual components may not provide an accurate picture of how each component contributes to the system as a whole. These strong interactions may also explain the significant spread in the decomposition of the BDC between the different wave components in the CCMVal2 model climatologies and climate change forecasts.

In section 2, we establish a new modeling framework to explore the interactions between the resolved waves and parameterized wave driving in a primitive equation model of the atmosphere. The model is forced with a highly simplified forcing that produces a realistic climate, as established by Held and Suarez (1994) and Polvani and Kushner (2002), but includes OGW and NOGW parameterizations from a state-of-the-art AGCM. The parameterized OGW driving is perturbed by varying one of its input parameters, as described in section 3, leading to substantial changes in the parameterized OGW driving in the midstratosphere. While an additive view of the BDC would then suggest a substantial change in the meridional overturning, the actual circulation changes very little, as the resolved wave driving nearly perfectly compensates for the perturbation in the parameterized OGW driving. A number of similar experiments suggest that the compensation is fairly robust to many changes in the OGW scheme and some changes in the NOGW scheme, supporting the findings of the McLandress and McFarlane (1993) study based on a quasi-linear QG model.

Analysis of the necessary condition for instability in the QG framework in section 4 suggests that the compensation is a response of the resolved waves to prevent instability in the flow driven by the parameterized OGW driving. Following the strategy of a ''proof by contradiction,'' we first suppose that the OGWD were not compensated. We then show that this leads to an

unstable mean state. This suggests that some degree of compensation is required to maintain a ''sensible'' residual-mean meridional circulation. The key factors determining the degree of compensation are the amplitude and meridional scale of the perturbation: stronger and narrower perturbations are more likely to be compensated. We then confirm the insight from the QG theory in a series of systematic experiments with the fully nonlinear primitive equation GCM.

Even in cases where the parameterized gravity wave driving is not compensated by the resolved waves (as explored in section 5), we find that the additive decomposition of the BDC into its wave-driven components can be misleading. The resolved waves can also respond strongly to changes in the mean state induced by changes in the gravity wave parameterization. The strong interactions between the parameterized waves and resolved waves again suggest that one must be careful when decomposing the BDC into wave-driven components. Last, our results summarized and discussed in the context of comprehensive AGCMs in section 6.

2. A new modeling framework

The AGCM used in this study was developed by the Geophysical Fluid Dynamics Laboratory (GFDL). It is exactly the same as that used in Polvani and Kushner (2002), except for a change in the gravity wave parameterization and a minor adjustment to the vertical coordinate. Briefly, the model integrates the dry hydrostatic primitive equations with pseudospectral numerics. The model is relaxed toward a simplified perpetual January radiative equilibrium temperature field to produce realistic tropospheric and stratospheric conditions without the need of convective or radiative schemes (Held and Suarez 1994; Polvani and Kushner 2002). In particular, the stratospheric relaxation temperature varies smoothly from the U.S. standard atmosphere over most of the stratosphere to a profile with constant lapse rate over the winter pole in order to produce a polar night jet. The strength of the polar night jet is controlled by a single parameter γ with typical values from 4 to 6 K km^{-1}; see Polvani and Kushner (2002) for details.

We focus on the Northern Hemisphere winter, as this is the period of maximal coupling between the troposphere and stratosphere on intraseasonal time scales. In the winter hemisphere, only large-scale planetary wave can efficiently propagate into the stratosphere owing to strong winds in the polar vortex (e.g., Charney and Drazin 1961). In the dynamical core framework, Gerber and Polvani (2009) showed that a simple large-scale topography is sufficient to excite an active stratospheric circulation. We use their configuration with most realistic coupling—a wavenumber-2 topography with 3-km amplitude between 25° and 65°N. The strength and structure of the BDC is controlled directly by the resolved topography and indirectly by the strength of the polar vortex. Gerber (2012) showed that increasing the amplitude of the resolved topography strengthens the planetary wave forcing and decreasing the temperature of the polar vortex (parameter γ) raises the planetary wave breaking region, hence deepening the circulation.

Polvani and Kushner (2002) included a crude parameterization for the mesospheric gravity wave driving by introducing a Rayleigh friction above 0.5 hPa, acting on the uppermost layers of the model, which extend to approximately 0.01 hPa. Drag near the model's top is needed to slow down the polar night jet, as the winds in radiative equilibrium exceed several hundred meters per second at these altitudes. We have replaced this crude parameterization with an interactive parameterization scheme for NOGW (Alexander and Dunkerton 1999) as implemented in GFDL's atmospheric model, version 3 (AM3; Donner et al. 2011). We use the same tuning parameters as in the AM3 settings: the momentum source is represented by a broad spectrum of wave speeds (half-width of 40 m s^{-1}) with a resolution of 2 m s^{-1} and a single horizontal wavelength of 300 km. The amplitude of the momentum source (see appendix) is 0.005 Pa in the Northern Hemisphere and 0.003 Pa in the Southern Hemisphere. The amplitude in the tropics is 0.004 Pa in AM3, but we reduce it by 95% in our dynamical core to eliminate permanent tropical zonal-mean zonal wind oscillations, a hint of which appears in the full atmospheric model (Donner et al. 2011, their Fig. 14). We note that the dry model, lacking convection parameterization, is fairly quiescent in the tropics. Including just part of the wave spectrum with the gravity wave parameterization leads to an unrealistic mean state. In addition, we have modified the NOGW scheme to conserve angular momentum, as discussed in the appendix.

OGW are parameterized as in GFDL's AM3 (Pierrehumbert 1987; Stern and Pierrehumbert 1988; Donner et al. 2011), except that we modify the scheme to conserve angular momentum, as discussed in the appendix. A key input parameter to the scheme is a measure of the subgrid-scale mountain height, which quantifies the amplitude of unresolved topography as discussed in detail in the following section 3.

All integrations in the study were completed with triangular truncation 42 resolution, corresponding roughly to a 2.8° grid and 40 hybrid vertical levels. Gerber and Polvani (2009) found that this resolution was sufficient to capture stratosphere–troposphere coupling. The vertical levels are spaced exactly as in Polvani and Kushner (2002), but we linearly transform from a pure

sigma coordinate at the surface to pure pressure coordinate above 200 hPa. Unless otherwise specified, experiments are integrated for 10 000 days, excluding 800 spinup days.

To gain confidence in the new model settings, we compare a few of the main stratospheric features of the old model configuration with the Rayleigh drag and $\gamma = 4\,\mathrm{K\,km^{-1}}$ (Gerber and Polvani 2009) to the new model configuration with just the NOGW parameterization and $\gamma = 6\,\mathrm{K\,km^{-1}}$. We have increased γ in order to get the same polar night jet structure, as the NOGW scheme produces more wave drag in the midstratosphere. The main characteristics of the zonal-mean zonal wind and residual-mean mass streamfunction circulation are similar. In particular, the forcing of the NOGW in the mesosphere (Fig. 1d) is similar to the forcing of the upper-layer Rayleigh drag (Fig. 1c). Note that in the new climate configuration the residual-mean mass circulation has deepened in the stratosphere (Figs. 1e,f). This was primarily caused by the increase in γ, which controls the strength of the polar vortex, as discussed in Gerber (2012).

Stratosphere–troposphere coupling, as measured by the frequency of stratospheric sudden warming (SSW) events (both minor and major), exhibits similar variability in both configurations—on average one major warming event every 200–300 days, consistent with the observed frequency of SSWs (Charlton and Polvani 2007), although all warmings are split vortex events, given the wavenumber-2 topographic forcing. The breakdown of the polar vortex at 10 hPa precedes a persistent shift of the tropospheric northern annular mode (NAM) toward a low-index state in the new model, as in observations (Baldwin and Dunkerton 2001). Last, the annular mode time scale of variability in the new model captures the observed increase in persistence in the lower stratosphere, as with the old configuration (Gerber and Polvani 2009). In summary, the new configuration preserves the key quantities of the stratosphere–troposphere system, but with an improved representation of gravity wave driving. The new model setting with its physically consistent NOGW parameterization and surface topography defines the default configuration of the study.

3. Compensation between resolved and parameterized wave driving

To study the interactions between resolved planetary waves and parameterized gravity waves, we intentionally perturb the OGW driving of the stratosphere. McLandress and McFarlane (1993) induced perturbations to the OGW driving in the mesosphere by suppressing interaction between their parameterization and the resolved flow and shifting the resolved planetary wave source. Focusing rather on the resolved flow, Gerber (2012) showed that the level of resolved wave breaking is influenced by the thermal forcing of the polar vortex, which sets zonal wind structure and thus the critical layer for stationary waves. In some analogy to both approaches, we perturb the OGW driving by shifting the location of the critical layer for stationary gravity waves through modification of an input parameter in the OGW scheme: the subgrid-scale mountain height, which represents the amplitude of unresolved topography.

The spatial structure of OGW source was chosen to have a global wavenumber-2 pattern with a peak amplitude of 240 m, as shown in Fig. 2. This broadscale pattern was chosen to maximize interactions with the resolved planetary waves, which were also forced at wavenumber 2. The amplitude was chosen to preserve the global average of the subgrid-scale topography height, as set in integrations of AM3 at equivalent horizontal resolution. With these choices, the phase angle between the resolved and subgrid-scale pattern is the sole remaining free parameter in the model. Here we focus on the extreme configurations, with the two patterns positively or negatively correlated. Additional experiments with intermediate configurations (not shown) revealed that these extremes captured the full range of interactions. In one extreme, the ''positive correlation'' configuration, we align the subgrid-scale mountain height with the ridges of the resolved topography (0° phase shift; Fig. 2a), while in the other, the ''negative correlation'' configuration, we shift the subgrid-scale mountain height to the valleys (180° phase shift; Fig. 2b).

Longitude–height cross sections of the zonal-mean zonal wind at the maximum amplitude of the resolved mountain (45°N) in Figs. 2c and 2d show how changing the phase between the resolved and unresolved topography modifies the OGWD. In the negative-correlation integration a critical layer for stationary waves (where $\overline{u} = 0$) is located in the stratosphere over the valleys, the OGW source region (Fig. 2d), while the wind remains positive at all levels over the ridges, the OGW source region in the positive-correlation integration (Fig. 2c). The effect of critical layers in the Pierrehumbert (1987) scheme is parameterized by limiting the flux by the square of the zonal velocity. It follows that the parameterized momentum flux generated in the negative-correlation integration dissipates lower in the stratosphere compared to the flux in the positive-correlation integration. Figure 3 shows the total impact of the phase shift on the time- and zonal-mean OGW driving. In the

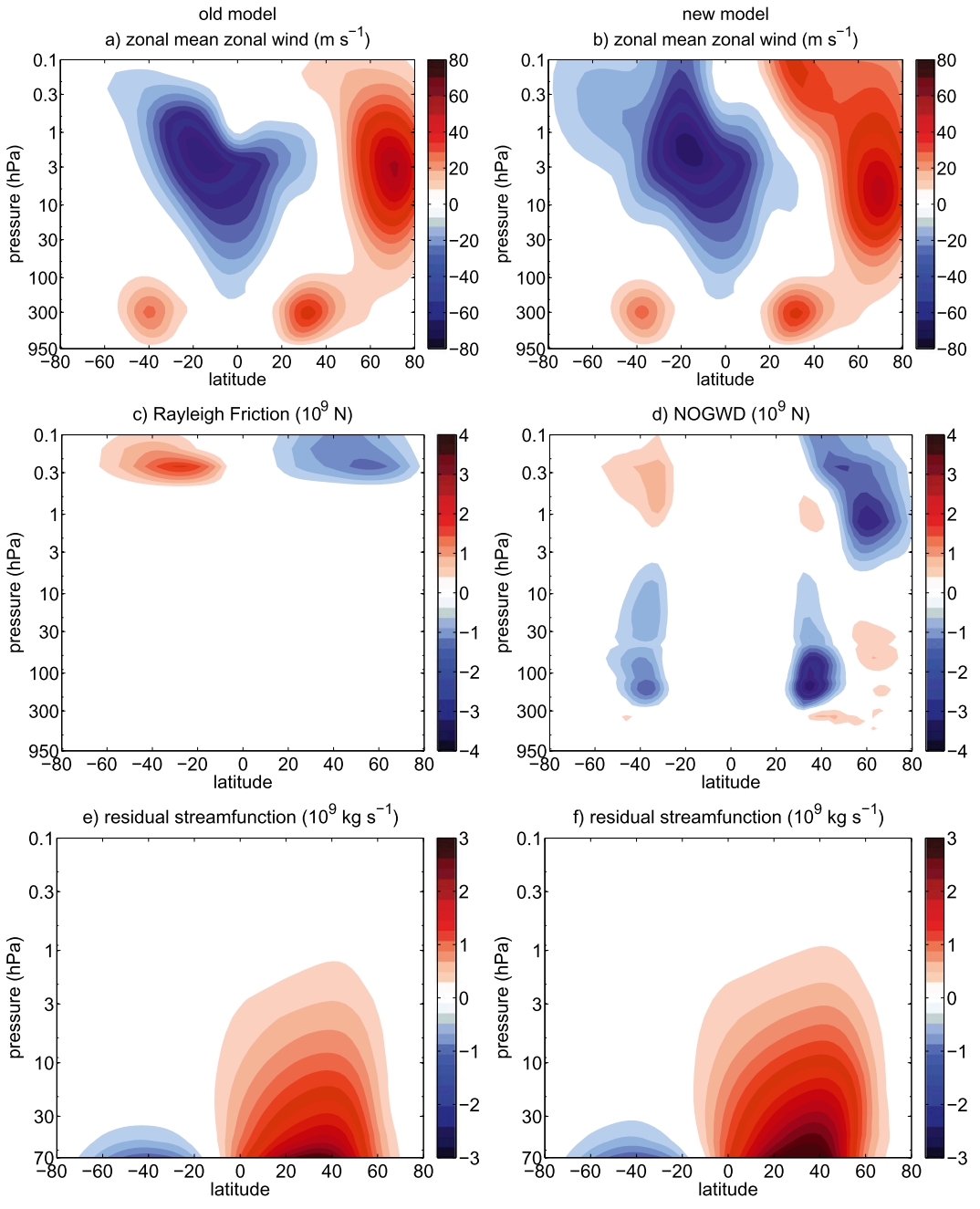

FIG. 1. A comparison between model configurations with Rayleigh friction, the "old" model used in Gerber and Polvani (2009), and the Alexander and Dunkerton (1999) NOGW parameterization, the "new" model used in this study: (a),(b) the time- and zonal-mean zonal winds (m s^{-1}), (c),(d) the time- and zonal-mean parameterized gravity wave driving (10^9 N), and (e),(f) the residual-mean mass streamfunction (10^9 kg s^{-1}).

negative-correlation integration (Fig. 3b), the parameterized wave driving is trapped in the lower stratosphere, and the wave driving above 70 hPa is extremely weak. In the positive-correlation integration (Fig. 3a), however, there is a substantial drag on the upper stratosphere.

The difference between the OGWD in the positive and negative integrations is shown in Fig. 4a. The amplitude of the zonally integrated perturbation is quite significant, on the order of 10^9 N, and can be put into context by considering the residual-mean mass circulation implied by downward control, as shown in Fig. 4b.

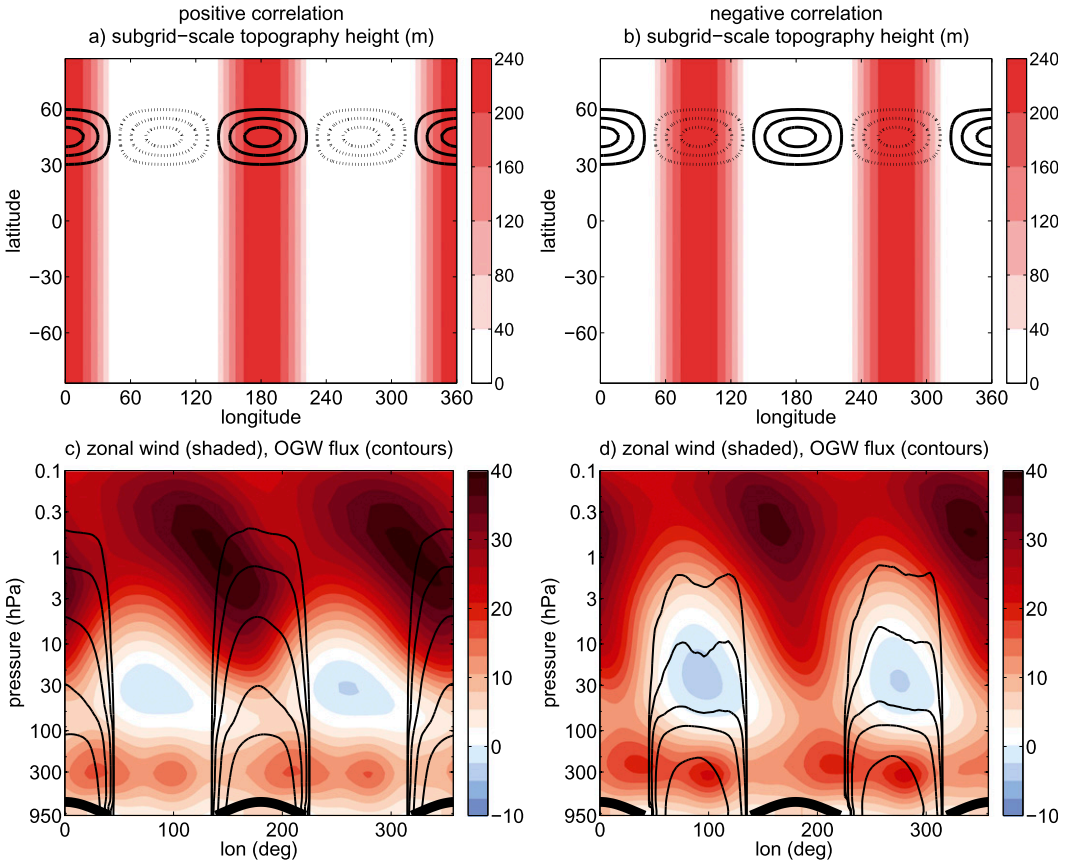

FIG. 2. The impact of the phase shift between the resolved and unresolved topography in the positive- and negative-correlation integrations. (a),(b) The structure of the resolved and unresolved topography. The black contours show the resolved, large-scale wavenumber-2 topography, with a maximum amplitude of 3 km; solid contours denote ridges and dashed contours denote valleys. The red shading shows the unresolved, wavenumber-2, subgrid-scale mountain height, which is an input parameter for the OGW scheme; the parameter is nonnegative, varying from 0 (white) to 240 m (darkest red shading), and quantifies the amplitude of unresolved topography within each grid box. (a) The positive-correlation configuration, where the subgrid-scale mountain height is largest over the ridges, and (b) the negative-correlation configuration, where the subgrid-scale mountain height is largest over the valleys. (c),(d) The time-mean zonal wind ($m\,s^{-1}$) as a function of longitude and height at 45°N. The thick black contours at the bottom of the figures denote the large-scale resolved topography and the black thin contours denote the OGW momentum flux, with contours varying from -3.5×10^{-3} to -3.5×10^{-7} Pa.

The total mass transport associated with this perturbation, assuming no change in the resolved wave driving, would be on the order of $10^9\,kg\,s^{-1}$, a substantial fraction of the total transport by the BDC, which is approximately $1.5 \times 10^9\,kg\,s^{-1}$ at 50°N and 70 hPa (as shown in Fig. 1e). The actual change in the residual circulation, however, is extremely weak, as illustrated in Fig. 4c. The residual circulation appears to ignore the torque entirely.

This does not, however, imply a problem with downward control, as one must also consider the response of the resolved wave driving. Figure 5a shows the difference in the resolved wave driving between the positive and negative integrations (i.e., the difference between Figs. 3c and 3d). It largely cancels out the OGW perturbation (Fig. 4a), so that the total change in wave forcing, $\Delta\overline{G}_{EPFD} + \Delta\overline{G}_{OGW} + \Delta\overline{G}_{NOGW}$, is very small. Note how this compares particularly well with the compensation observed in the mesophere by McLandress and McFarlane (1993, their Fig. 10), where they compared integrations in which the interaction between the parameterized wave drag and the resolved flow was toggled on and off. Fourier decomposition of the EPFD in both integrations reveals that the response of the resolved waves to the OGW perturbation, as quantified by the difference in the EPFD, is dominated by planetary wavenumber 2 (Fig. 5b). Overall, the result is that the net forcing on the stratosphere is almost the same in the positive- and negative-correlation integrations, and

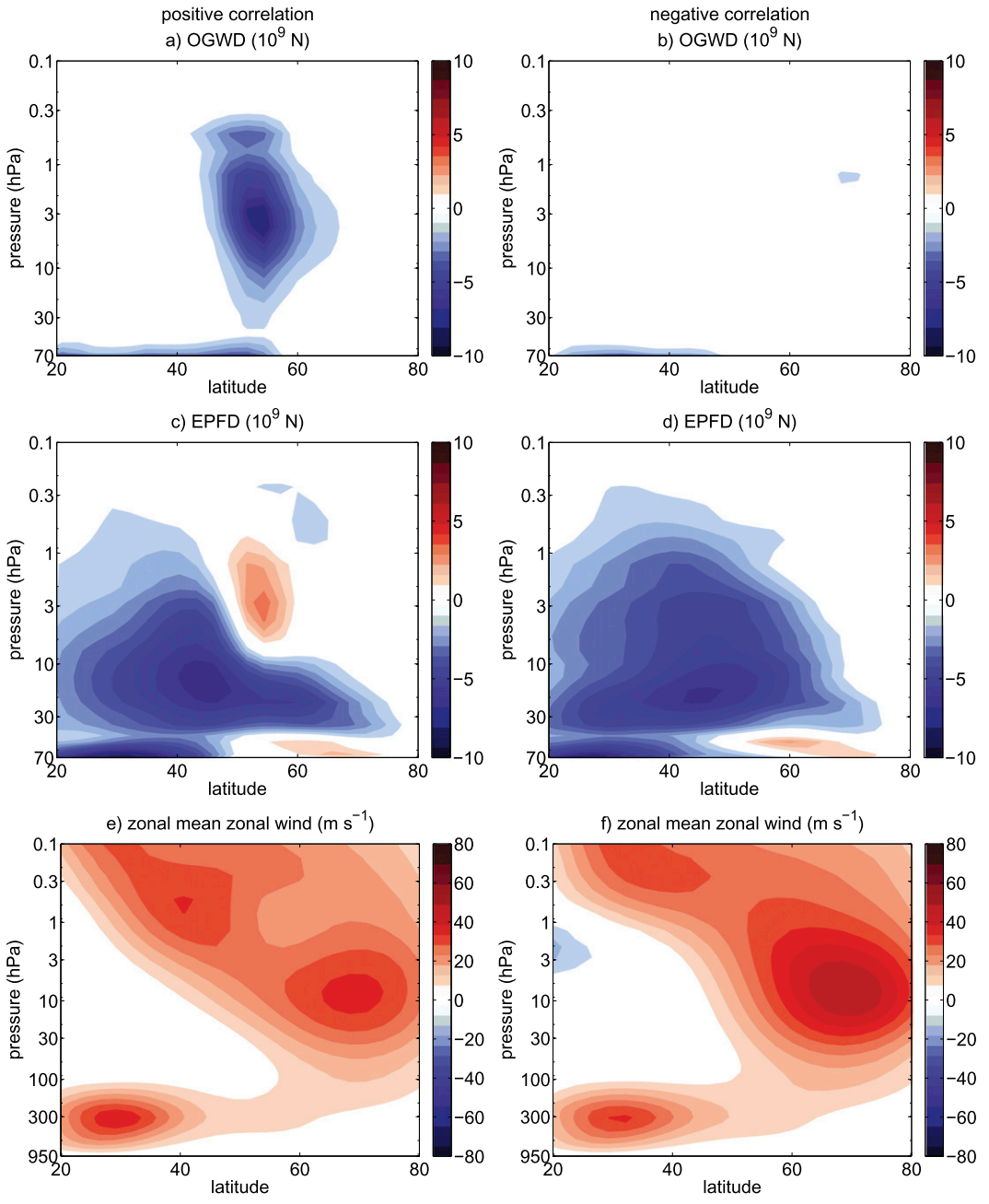

FIG. 3. (top) The time- and zonal-mean OGW driving $\overline{G}_{\mathrm{OGW}}$ in the (a) positive-correlation and (b) negative-correlation integrations (10^9 N); (middle) the time- and zonal-mean EPFD $\overline{G}_{\mathrm{EPFD}}$ in the (c) positive-correlation and (d) negative-correlation integrations (10^9 N); and (bottom) the time- and zonal-mean zonal wind $\overline{u}$ in the (e) positive-correlation and (f) negative-correlation integrations (m s^{-1}).

consequently the meridional overturning circulation does not change as shown in Fig. 4c.

As highlighted in Figs. 3e and 3f, however, the change in OGW driving does have a significant impact on the zonal-mean zonal wind. The difference in the zonal winds is shown in Fig. 4d, revealing a dipole structure of amplitude 20 m s^{-1} centered about the OGWD perturbation. Close inspection of the OGWD and EPFD fields (Figs. 4a and 5a) reveals that while compensation is nearly exact at the center of the OGW perturbation, there are slight differences on the flanks. As also observed by McLandress and McFarlane (1993), the zonal wind is more sensitive to changes in the momentum budget than the meridional overturning circulation.

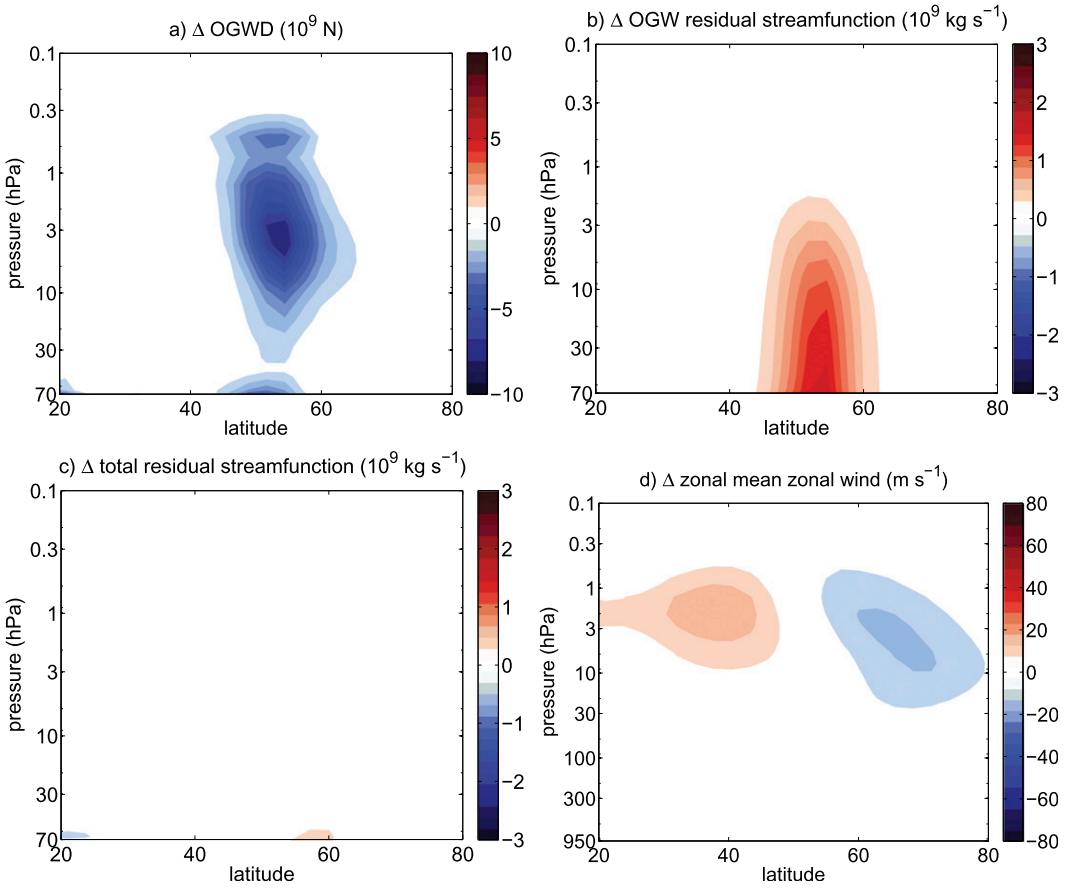

FIG. 4. (a) The difference in the time- and zonal-mean OGW driving $\Delta\overline{G}_{\mathrm{OGW}}$ between the positive- and negative-correlation integrations (10^9 N). (b) The difference in the residual circulation $\Delta\overline{\psi}^*_{\mathrm{OGW}}$ (10^9 kg s^{-1}) associated with the difference in the OGW driving, as computed by downward control. (c) The difference in the total residual circulation $\Delta\overline{\psi}^*_{\mathrm{Tot}}$ (10^9 kg s^{-1}) and (d) the difference in the zonal-mean zonal wind $\Delta\overline{u}$ (m s^{-1}).

Figure 6 shows the residual-mean streamfunction at 70 hPa for the negative and positive integrations. While these integrations essentially have the same meridional circulation, they tell a very different story on the relative importance of the resolved and parameterized waves to the stratospheric mass transport. In the positive-correlation integration (Fig. 6a), orographic gravity waves drive over half of the stratospheric mass flux across 50°N, while in the negative-correlation integration (Fig. 6b), they play an insignificant role. Viewed together, however, these plots suggest that either interpretation is likely to be misleading. The total circulation is about the same in both integrations, despite large changes in the OGW scheme, suggesting that large-scale constraints govern the total meridional overturning circulation.

Robustness of the compensation response

We define a heuristic measure for the compensation that can be applied for different perturbation integrations. In general, given a perturbation P to a system in equilibrium, the system may react with a response R in order to equilibrate again. In the following, we define a measure that aims to quantify the relation between the perturbation and the response. In our system, $P(x_i)$ is a perturbation to the zonal-mean wave driving, where x_i is a generic spatial coordinate. The response $R(x_i)$ is defined as the net change in the other components of the zonal wave driving. For example, in the positive- and negative-correlation integrations shown in Figs. 2–6, $P = \Delta\overline{G}_{\mathrm{OGW}}$, the change in the OGWD, and $R = \Delta\overline{G}_{\mathrm{EPFD}} + \Delta\overline{G}_{\mathrm{NOGW}}$, the change in the EPFD and the NOGWD. The degree of compensation C between the P and R is defined as the scaled covariance between the perturbation and the response,

$$C = 1 - \frac{\sum_i [P(x_i) + R(x_i)]^2}{\sum_i P^2(x_i) + \sum_i R^2(x_i)} = -\frac{2\sum_i [P(x_i)R(x_i)]}{\sum_i P^2(x_i) + \sum_i R^2(x_i)}, \tag{1}$$

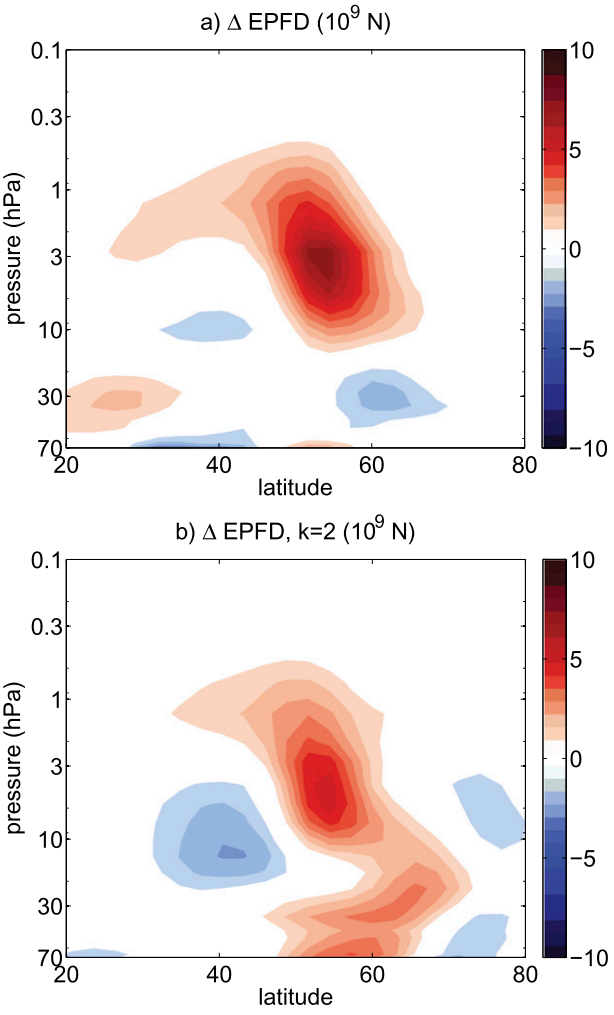

FIG. 5. (a) The difference in the resolved wave forcing $\Delta\overline{G}_{\mathrm{EPFD}}$ between the positive- and negative-correlation integrations in the time and zonal mean (10^9 N). (b) The contributions of planetary wavenumber 2 to the difference in the resolved wave forcing (10^9 N).

where the summation is constraint to the region in which $|P(x_i)| > 0.1 \max_i |P(x_i)|$. The threshold of 0.1 is established so that C is measured only in the region where $|P|$ is greater than 10% of its maximum absolute value. This was done because in regions where the perturbation is weak, noise in the response can obscure the signal. We also restrict our analysis to regions above 70 hPa, as changes in the upper troposphere–lower stratosphere can overwhelm the rest of the stratosphere.

With this definition, if the response is equal and opposite to the perturbation (i.e., $R = -P$), we have perfect compensation and $C = 1$. If $R = 0$, or more generally is uncorrelated with the perturbation, then $C = 0$ (there is no compensation) and if $R = P$, then $C = -1$; the system amplifies the perturbation. In the case of the positive- and negative-correlation integrations we observe a high degree of compensation: $C = 0.95 \pm 0.01$. This case is labeled as "control run" in Fig. 7. We emphasize that this metric best reflects changes in the meridional overturning circulation; even at 0.95, differences in the total wave forcing in these interactions does lead to nontrivial changes in the zonal wind, as seen in Figs. 3e and 3f.

The uncertainty of the compensation was computed using the bootstrap and the moving-blocks bootstrap methods (Efron and Tibshirani 1994; Wilks 1997). We used the bootstrap with 200-member resampling and the moving-blocks method with 200 resamples and a block size of 100 days in order to retain the time correlation in the data. The different methods yield almost identical results; thus we will show only the former. Although it turns out that the need to bootstrap the data to determine the uncertainty is insignificant when the compensation is high, it is important for cases of weak compensation. For example, when one tries to assess the effect of a weak wave forcing, the natural variability can more easily overwhelm the forcing effect.

We first verify that compensation is not an artifact of resolution. Integrations with double the vertical resolution (80 levels) and with double horizontal resolution (T85 spectral truncation) yield a virtually identical degree of compensation between the positive-and negative-correlation integrations.

We next verify that the compensation is not an artifact of the particular wavenumber-2 topography of our default configuration integrations. In particular, McLandress and McFarlane (1993) focused on the mesosphere, where zonal asymmetries are dominated by wavenumber 1. We run similar simulations, but with lower boundary settings of wavenumber 1 ($k = 1$) and wavenumber 3 ($k = 3$), keeping the same amplitude of 3 km. [Similar configurations were explored in Gerber and Polvani (2009).] The subgrid-scale mountain height parameter is given a large-scale pattern with the same wavenumber k as the resolved topography, again with a maximum height of 240 m. We consider cases with positive correlation (where the resolved and unresolved topographies align with each other) and negative correlation (ridges align with the valleys). As before, P and R are the difference in $\overline{G}_{\mathrm{OGW}}$ and $\overline{G}_{\mathrm{EPFD}} + \overline{G}_{\mathrm{NOGW}}$ between the positive-correlation and negative-correlation integrations (see Table 1). Figure 7 (see labels "$k = 1$" and "$k = 3$") show that there is a consistently high degree of compensation in these experiments. We can conclude that the compensation is a fairly generic feature in the model.

Holton (1984) suggested that the spatial variation of the OGWD can lead to the generation of planetary

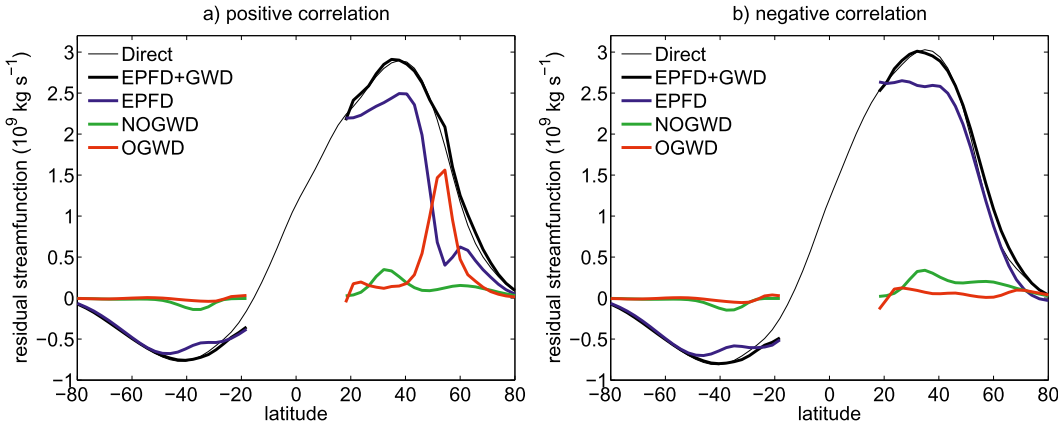

FIG. 6. The residual-mean streamfunction at 70 hPa, as a function of latitude, for the (a) positive-correlation and (b) negative-correlation integrations (10^9 kg s^{-1}). "Direct" refers to the total residual-mean streamfunction computed directly from the definition of the residual-mean velocities. "EPFD+GWD" refers to the total residual-mean mass streamfunction computed by downward control, while "EPFD," "NOGWD," and "OGWD" refer to the residual-mean streamfunctions associated with each of the wave components: resolved, nonorographic, and orographic gravity wave driving (the thick black curve is thus the sum of the blue, green, and red curves).

waves in the mesosphere. Even though the wave driving is determined separately for each column, the structure of the subgrid-scale mountain height parameter gives the resulting drag significant zonal structure relative to the climatological stationary planetary waves as seen—for example, in our integrations in Figs. 2c and 2d. The parameterized wave forcing can thus be a source of planetary waves, providing a resolved Eliassen–Palm flux divergence that could compensate the parameterized torque. McLandress and McFarlane (1993) found further evidence for the generation of planetary waves by the OGWD, although their analysis suggested a different mechanism than initially proposed by Holton (1984).

To assess the significance of the spatial and temporal structure of the parameterized wave driving, we turned off the OGW parameterization and ran simulations using a steady specified torque derived from the OGW forcing of the positive-correlation (with $k = 2$) simulation. Specifically, we ran three simulations with specified forcing by applying (i) the time mean and (ii) the time and zonal mean, and by (iii) using the time-mean forcing but shifting its phase by 180°. Note that the latter experiment is similar, in structure, to the sensitivity case D in McLandress and McFarlane (1993), except that they instead shift the resolved waves. Figure 7 (see labels "time-mean forcing," "time- and zonal-mean forcing,"

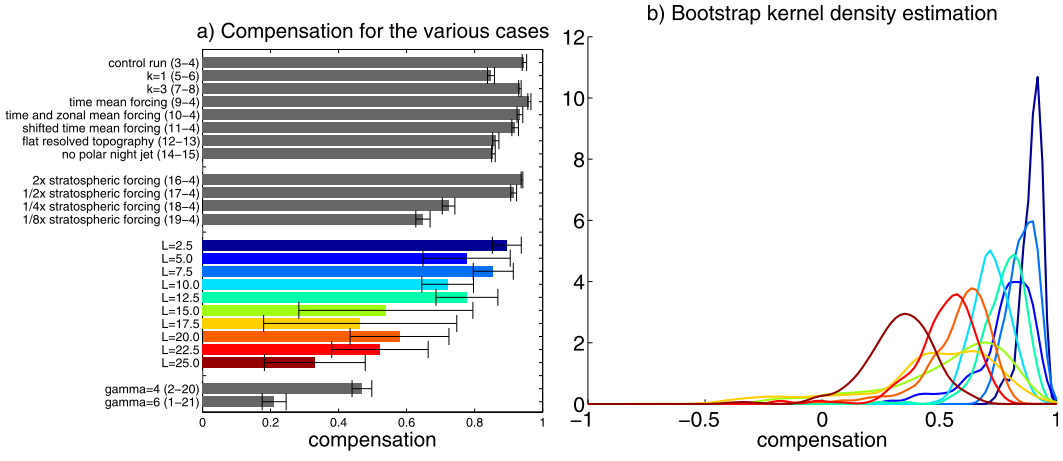

FIG. 7. (a) The compensation metric C for the various integrations. Each bar corresponds to a difference between two integrations as listed in Table 1. For example, the control run is the difference between integrations 3 and 4 in Table 1. The error bars correspond to one standard deviation in C. (b) The bootstrap kernel density estimate for the integrations labeled by "$L = 2.5$," "$L = 5.0$," . . . , "$L = 25.0$." The colored bars in (a) and the colored curves in (b) match.

TABLE 1. Summary of the configurations for the different integrations, where an overbar denotes a zonal mean and square brackets denote a time mean. In the second-to-left column, the wavenumber and phase shift, relative to the resolved topography, of the pattern governing the subgrid-scale topography height (SSTH) is specified. In the right column, [int. 3] refers to the time-mean OGW torque from integration 3, and so forth. Multiplication by 2, ½, ¼, and ⅛ denotes that the forcing above 70 hPa was multiplied by 2, ½, ¼, and ⅛.

Integration number	Integration name	γ	Wavenumber, resolved topography	Rayleigh drag	NOGW	OGW	SSTH wavenumber (phase shift)	Prescribed torque
1	Default "new" model	6	2		✓			
2	Default "old" model	4	2	✓				
3	Positive correlation with $k = 2$	6	2		✓	✓	2 (0°)	
4	Negative correlation with $k = 2$	6	2		✓	✓	2 (180°)	
5	Positive correlation with $k = 1$	6	1		✓	✓	1 (0°)	
6	Negative correlation with $k = 1$	6	1		✓	✓	1 (180°)	
7	Positive correlation with $k = 3$	6	3		✓	✓	3 (0°)	
8	Negative correlation with $k = 3$	6	3		✓	✓	3 (180°)	
9	Time mean, positive correlation with $k = 2$	6	2		✓			[int. 3]
10	Time and zonal mean, positive correlation with $k = 2$	6	2		✓			$[\overline{\text{int.3}}]$
11	Shifted time mean, positive correlation with $k = 2$	6	2		✓			[int. 3] (90°)*
12	Flat, positive correlation	6	Flat		✓			[int. 3]
13	Flat, negative correlation	6	Flat		✓			[int. 4]
14	No polar night jet, positive correlation	—	2		✓			[int. 3]
15	No polar night jet, negative correlation	—	2		✓			[int. 4]
16	2× stratospheric forcing, positive correlation	6	2		✓			2 [int. 3]
17	0.5× stratospheric forcing, positive correlation	6	2		✓			(1/2) [int. 3]
18	0.25× stratospheric forcing, positive correlation	6	2		✓			(1/4) [int. 3]
19	0.125× stratospheric forcing, positive correlation	6	2		✓			(1/8) [int. 3]
20	"New" model with $\gamma = 4$	4	2		✓			
21	"Old" model with $\gamma = 6$	6	2	✓				

* In this integration, the time-mean torque from integration 3 was shifted by 90°.

and "shifted time-mean forcing") shows, however, that each of these experiments exhibits the same high degree of compensation: the time-mean forcing experiment suggests that variability of the OGW in time is not important, and the zonal-mean and shifted time-mean experiments suggest that the zonal structure is also not important. The case in which the OGW forcing is applied as a time- and zonal-mean torque, in particular, rules out the possibility that compensation depends on the generation of planetary waves by the parameterized torque.

While the structure of the OGWD does not appear to matter, a second question is how the structure of the resolved waves and background flow affect the compensation. We address this question by altering the planetary wave source and by modifying the mean state of the stratosphere, hence changing the propagation properties of the planetary waves.

In the first experiment, we alter the topographic planetary wave source by removing the large-scale topography, consequently reducing the stratospheric planetary wave activity and decreasing planetary waves breaking in the stratosphere (Gerber 2012). This is similar to the sensitivity case C in McLandress and McFarlane (1993), where they suppressed the resolved wave forcing. In the second experiment we modify the mean state of the stratosphere. Using the parameter γ, we completely remove the polar night jet, so that the planetary waves dissipate or reflect before they can enter the stratosphere (Gerber and Polvani 2009). To prevent the OGW from changing, we specify a steady torque equal to the time-mean OGW driving from the positive-correlation integration (with $k = 2$), and compare this integration to an integration with the time-mean OGW driving from the negative-correlation integration (with $k = 2$) (see Table 1). Figure 7 (see labels

''flat resolved topography'' and ''no polar night jet'') show almost perfect compensation for these two experiments. It follows that the climatological structure of the resolved waves plays also only a limited role in the compensation process.

Last, we test how the amplitude of the parameterized forcing affects the compensation. We increase/decrease the stratospheric prescribed time-mean forcing and observe the change in compensation. We run four simulations in which we use again the time-mean OGW driving from the positive-correlation integration with $k = 2$, but with double, half, one-quarter, and one-eighth the time-mean stratospheric forcing above 70 hPa. Perturbation will be defined as before, by comparing to an integration with the time-mean forcing from the negative-correlation integration (see Table 1). Figure 7 (see labels ''2×,'' ''1/2×,'' ''1/4×,'' and ''1/8× stratospheric forcing'') shows that the compensation decreases as the amplitude of the OGW perturbation decreases.

To summarize, our integrations show that resolved Rossby waves act to compensate perturbation of the parameterized OGW, so that the residual-mean mass circulation does not change. We find that the process is fairly robust to significant changes in both the OGW and the resolved wave driving, suggesting that the mechanism does not depend on the zonally asymmetric structure of the flow or the OGW. It is only weakened when we reduce the amplitude of the perturbation. At first, the last group of results puzzled us, as it appears that there is less compensation in instances when the resolved waves have less of a perturbation to compensate. However, the fact that compensation becomes weaker for weaker perturbations led us to suspect that the OGW forcing may be generating instability. A hint can be seen in Fig. 3c, where a positive EPFD is located at the region of compensation, suggesting a source of wave activity in the stratosphere. Thus, we hypothesize that compensation occurs when the parameterized forcing destabilizes the stratosphere and that the planetary waves adjust to it in order to stabilize the flow again. In the next section, we examine this hypothesis by studying the necessary condition for instability as a function of the wave driving using the QG TEM equations.

4. Constraints on the wave driving in the QG TEM equations

We will proceed largely by developing a proof by contradiction. We suppose that there is no compensation between the resolved and unresolved waves and show that the resulting zonal-mean flow is unstable. Thus, the resolved meridional circulation must respond to maintain stability. We find that it does so, producing resolved wave forcing that is roughly equal and opposite to the parameterized wave forcing.

a. Theory

A necessary condition for instability in the QG framework is that the zonal-mean meridional QG potential vorticity (QG-PV) gradient changes sign somewhere in the domain. Denoting the zonal-mean PV by $\overline{q}$, in Cartesian pressure coordinates (x, y, p) the QG-PV gradient is

$$\overline{q}_y = \beta - \overline{u}_{yy} - (\epsilon \overline{u}_p)_p . \tag{2}$$

Terms on the right-hand side correspond to the meridional gradient in the planetary vorticity, relative vorticity, and vorticity stretching, respectively (e.g., Edmon et al. 1980; Vallis 2006). An overbar represents a zonal mean and a subscript a partial derivative, $\beta = 2\Omega \cos\phi_0/a$, where Ω is Earth's angular velocity, ϕ is the latitude, ϕ_0 is a reference latitude, a is Earth's radius, u is the zonal wind, and ϵ is a related to the stratification and discussed in further detail below. We follow the downward control argument (Haynes et al. 1991) to compute the zonal-mean flow (winds and temperature) in response to a steady wave driving. The goal is to express the necessary condition for instability in terms of the wave driving alone. In this way we can determine whether a steady stable solution is possible for a given parameterized wave driving.

The steady QG-TEM equations with simple Newtonian relaxation of the temperature are (e.g., Andrews and McIntyre 1978; Edmon et al. 1980)

$$-f_0 \overline{v}^* = \overline{G}, \tag{3a}$$

$$\overline{v}^*_y + \overline{\omega}^*_p = 0, \tag{3b}$$

$$\overline{\omega}^* \overline{\theta}_p + \frac{\overline{\theta} - \theta_r}{\tau_r} = 0, \quad \text{and} \tag{3c}$$

$$f_0 \overline{u}_p - \frac{p^{\kappa-1} R}{p_0^{\kappa}} \overline{\theta}_y = 0, \tag{3d}$$

where $f_0 = 2\Omega \sin\phi_0$ is the Coriolis acceleration, $\overline{v}^*$ and $\overline{\omega}^*$ are the residual-mean meridional and vertical winds, $\overline{G}$ is the zonal-mean wave driving, and $\overline{\theta}$ is the zonal-mean potential temperature, assuming $\overline{\theta}_p = \overline{\theta}_p(p)$ (Andrews et al. 1983). Also, θ_r is the radiative equilibrium potential temperature that is in thermal wind balance with zonally uniform wind field u_r, τ_r is the relaxation time scale, and ϵ in (2) is $\epsilon = -f_0^2 p \overline{\theta}/R\overline{T}\overline{\theta}_p$; ϵ is a function of p alone, is strictly positive, and captures changes in the stratification. Finally, $p_0 = 10^3$ hPa,

$\kappa = R/c_p \approx 2/7$, where c_p is the specific heat at constant pressure, and R is the dry gas constant.

Following the downward control derivation, using (3a) in (3b) we get

$$\overline{v}^* = -\frac{\overline{G}}{f_0} \Rightarrow$$
$$\overline{\omega}^*(y,p) = \frac{1}{f_0}\int_{p_1}^{p} \overline{G}_y(y,s)\,ds + \overline{\omega}^*(y,p_1). \qquad (4)$$

Taking the y derivative of (3c) and using (4) yields

$$(\theta_r - \overline{\theta})_y = \tau_r \overline{\omega}^*_y \overline{\theta}_p$$
$$= \frac{\tau_r \overline{\theta}_p}{f_0}\int_{p_1}^{p} \overline{G}_{yy}(y,s)\,ds + \tau_r \overline{\theta}_p \overline{\omega}^*_y(y,p_1). \qquad (5)$$

Multiplying (5) by $f_0/\overline{\theta}_p$ and taking the p derivative gives

$$\tau_r \overline{G}_{yy} = f_0\left[\frac{(\theta_r - \overline{\theta})_y}{\overline{\theta}_p}\right]_p = [\epsilon(\overline{u} - u_r)_p]_p, \qquad (6)$$

where the equality on the right follows using (3d). Equation (6) provides the essence of the downward control: the mean flow fields $\overline{\theta}$ and $\overline{u}$ are solely determined by the wave forcing $\overline{G}$ (up to a boundary term).

In a stable dynamically equilibrated stratosphere, the background $\overline{q}_y$ is positive (e.g., in regions with no shear flow, $\overline{q}_y = \beta > 0$) and so we write the necessary condition for instability as $\overline{q}_y < 0$. Let us consider a mean wave driving $\overline{G}_0$ that determines the zonal-mean fields $\overline{u}_0$ and $\overline{\theta}_0$ such that $\overline{q}_y = \overline{q}_{0y} \geq 0$, where $\overline{q}_0$ denotes the zonal-mean QG-PV of the mean state. For example, Fig. 8 shows $\overline{q}_{0y}$ over the Northern Hemispheric stratosphere for the default integration with the NOGW (simulation 1 in Table 1); $\overline{q}_{0y}$ is strictly positive and its overall amplitude is on the order of β. Now, consider a perturbation to the stable system. We denote the perturbed wave driving as $\overline{G}_1$ and the resultant flow as $\overline{u}_1$ and $\overline{\theta}_1$. Under the assumption that the wave forcing is linearly additive, with no interactions between the wave forcings, $\overline{G} = \overline{G}_0 + \overline{G}_1$, the necessary condition for instability in (2) becomes

$$\overline{q}_y = \overline{q}_{0y} + \overline{q}_{1y} < 0 \Rightarrow \overline{q}_{0y} < \overline{u}_{1yy} + (\epsilon \overline{u}_{1p})_p, \qquad (7)$$

where $\overline{q}_{1y}$ is defined to be

$$\overline{q}_{1y} \equiv -\overline{u}_{1yy} - (\epsilon \overline{u}_{1p})_p. \qquad (8)$$

In words, the necessary condition for instability is that the perturbed QG-PV meridional gradient overwhelms the existing meridional gradient. Equation (6) can be separated for a basic-state balance governed by $\overline{G}_0$ and a balance due to the perturbation $\overline{G}_1$, where the latter balance is

$$\tau_r \overline{G}_{1yy} = (\epsilon \overline{u}_{1p})_p. \qquad (9)$$

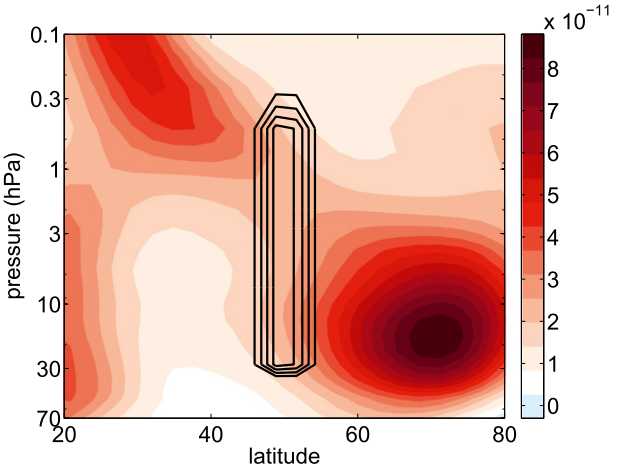

FIG. 8. The time and zonal mean of the meridional gradient of the QG-PV $\overline{q}_{0y}$ ($\mathrm{m^{-1}\,s^{-1}}$) in the default integration with the NOGW and $\gamma = 6\,\mathrm{K\,km^{-1}}$. The black contours denote the location and strength of the wave forcing $\overline{G}_1$ discussed in section 4.

Using standard dimensional analysis technics (e.g., Barenblatt 1996), let the perturbed wave driving $\overline{G}_1$ scale with amplitude A, let L and H be the meridional and vertical scales on which the wave driving varies, respectively, and let $\overline{u}_1$ scale with U. The scale of the background QG-PV gradient $\overline{q}_{0y}$ is denoted as Q_y. To make analytical progress, we simplify ϵ by assuming constant stratification $N^2 = -g^2\rho\overline{\theta}_p/\overline{\theta}$ and that the temperature is equal to the reference temperature $\overline{T} = T_0$. Thus, ϵ simplifies to $(f_0 g p/RT_0 N)^2 = (p/L_d)^2$, where $L_d = NH_\rho/f_0$ is the Rossby radius of deformation and $H_\rho = RT_0/g$ is the density height scale. It follows from (9) that $\overline{u}_1$ scales as

$$\overline{u}_1 \propto U \propto \tau_r A \frac{L_d^2}{L^2}\frac{H^2}{H_\rho^2}. \qquad (10)$$

The same scaling analysis can be found in Garcia (1987) and Haynes et al. (1991), though in the latter they denote L_d/L as H_ρ/H_R, where $H_R = f_0 L/N$ is the "Rossby height" for the problem. Using (9) and (10), we scale each term in the necessary condition for instability [(7b)] to get

$$Q_y < \frac{\tau_r A}{L^2}\max\left\{\frac{L_d^2}{L^2}\frac{H^2}{H_\rho^2}, 1\right\}. \qquad (11)$$

Note that the factor $L_d^2 H^2/L^2 H_\rho^2$ is the ratio between the amplitude of the QG-PV associated with meridional

gradient in the relative vorticity $-\overline{u}_{1yy}$ and vortex stretching $-(\epsilon\overline{u}_{1p})_p$.

- For $L \gg L_d$, when L is large compared to the Rossby radius of deformation, the vertical gradient in $\overline{u}_1$, associated with the vortex stretching, dominates the PV gradient and (11) yields a simple condition on the necessary condition for instability:

$$A > \frac{Q_y L^2}{\tau_r}. \tag{12}$$

  In this limit the amplitude must be fairly large to satisfy the necessary condition for instability.
- For $L \ll L_d$, when L is small compared to L_d, the relative vorticity gradient dominates and (11) yields the following necessary condition for instability:

$$A > \frac{Q_y L^4}{\tau_r L_d^2}\frac{H_\rho^2}{H^2}. \tag{13}$$

  Here, the critical amplitude for instability decreases rapidly with the meridional scale of the perturbation, and so is extremely sensitive to L. In addition, the critical amplitude is inversely proportional to the square of the wave forcing height scale: the larger the vertical extent, the smaller the critical amplitude for instability.
- If $L = L_d$ and $H = H_\rho$, the condition is

$$A \equiv A_c = \frac{Q_y L_d^2}{\tau_r}. \tag{14}$$

  If we suppose that Q_y scales as β, then we get a rough estimate of the critical amplitude $A_c \approx 8 \times 10^{-6}\,\mathrm{m\,s^{-2}} \approx 1\,\mathrm{m\,s^{-1}\,day^{-1}}$, based on the parameters consistent with our model, $N = \sqrt{5} \times 10^{-2}\,\mathrm{s^{-1}}$, $H = 7\,\mathrm{km}$, $\tau_r = 40$ days, and where the torque is centered around $\phi = 50°\mathrm{N}$.

When A and L are such that $\overline{q}_{0y} + \overline{q}_{1y} < 0$, as in (7a), the only way that a stable equilibrated limit can be achieved is if a resolved wave driving is generated such that

$$\overline{q}_{0y} + (\overline{q}_{1y} + \overline{q}_{Ry}) > 0, \tag{15}$$

where $\overline{q}_R$ stands for the contribution of a perturbed resolved Rossby wave to the QG-PV meridional gradient. In an OGW parameterization, L is set primarily by the spatial extent of the subgrid-scale mountain height and surface winds. In practice, both tend to vary on a much shorter scale than the deformation radius L_d of the stratosphere, which is about 50% larger than in the troposphere because of increased stratification. Typical amplitudes for the OGWD are on the order of $1\,\mathrm{m\,s^{-1}\,day^{-1}}$ (Alexander et al. 2010), thus the necessary condition for instability is quite likely to be satisfied.

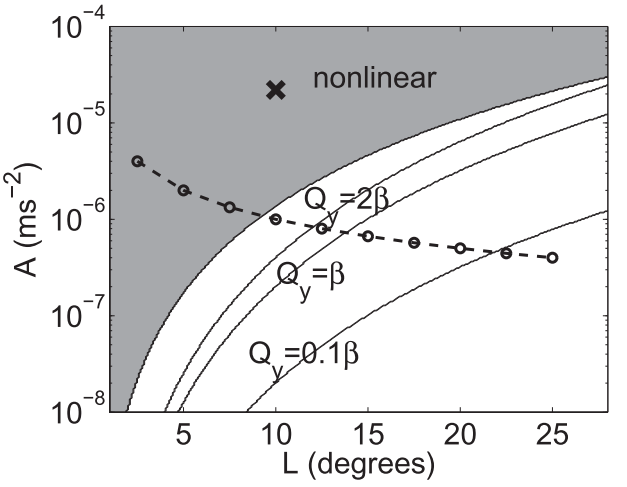

FIG. 9. The necessary condition for instability, as in (11), as a function of the wave driving's amplitude A, meridional extent L, and background PV gradient Q_y, where $\tau_r = 40$ days, $N = \sqrt{5} \times 10^{-2}\,\mathrm{s^{-1}}$, $H = 29\,\mathrm{km}$, centered at $\phi_0 = 50°$. The solid lines correspond to instability thresholds for $Q_y = 0.1\beta$, β, and 2β. To the lower-right, the flow is likely to be stable and to the upper left, the flow is likely to be unstable. The shaded gray area indicates the nonlinear region where the downward control limit is no longer applicable. The open circles indicate the different A and L values that we explored in our AGCM. The thick cross denotes the amplitude and meridional scale of the perturbation generated by the GFDL OGW scheme, shown in Figure 3a.

As discussed above, Haynes et al. (1991) denoted L_d/L as H_ρ/H_R, because $L_d/L = NH_\rho/f_0 L = H_\rho/H_R$. Inspection of (8) and (11) reveals that the necessary condition for instability depends on the second and fourth meridional derivatives of the wave forcing, hence we believe that L_d/L is a better instability measure then H_ρ/H_R.

Figure 9 sketches out where the necessary condition for instability in (11) is satisfied as a function of the wave driving amplitude and length, using $Q_y = 0.1\beta$, β, and 2β, where $\tau_r = 40$ days, $N = \sqrt{5} \times 10^{-2}\,\mathrm{s^{-1}}$, $H = 29\,\mathrm{km}$, and the forcing is centered at $\phi_0 = 50°$ such that $L_d \approx 13°$. Clearly, Q_y has a stabilizing effect; the larger it is, the more stable the flow is. The nonlinear shaded gray indicates the region where the Rossby number exceeds 1, hence the QG approximation breaks down and the QG downward control limit is no longer applicable. Note, however, that the flow is likely to go unstable before it reaches this limit. The boldface cross in the figure denotes the amplitude and meridional scale of the perturbation generated by the GFDL OGW scheme, shown in Fig. 3a. Clearly, this wave forcing had to be compensated to yield a sensible mean state.

b. *Verification of the theory in the model*

We next test the hypothesis that compensation is related to instability in our AGCM, where we can explore

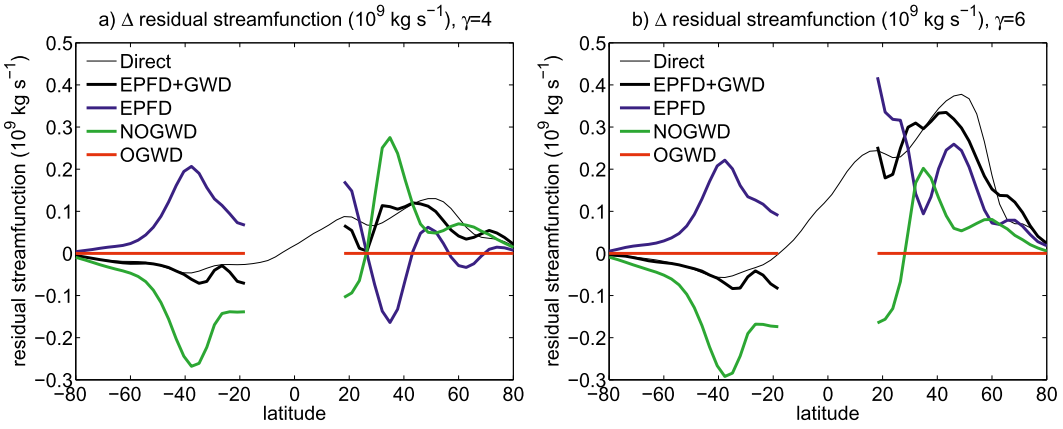

FIG. 10. The residual-mean streamfunction (10^9 kg s^{-1}) at 70 hPa, as a function of latitude, showing the difference between an integration with NOGWD and a similar simulation with the Rayleigh drag, with (a) $\gamma = 4$ and (b) $\gamma = 6$ K km^{-1}. The labels correspond to Fig. 6.

the sensitivity of compensation to the amplitude A and meridional scale L of the perturbation. We consider a specific example in which the wave driving perturbation $\overline{G}_1$ is

$$\overline{G}_1(y,p) = \begin{cases} -\dfrac{A}{2}\{1+\cos[\pi(y-y_0)/L]\}, & \text{if} \quad |y-y_0| \le L, p1 \le p \le p_2 \\ 0, & \text{otherwise.} \end{cases} \tag{16}$$

This compactly supported wave forcing $\overline{G}_1$ is shown by the black contours in Fig. 8, for a case with $A = 2 \times 10^{-6}$ m s^{-2}, $L = 5°$, $p_1 = 0.5$ hPa and $p_2 = 30$ hPa (such that $H = 29$ km), centered around $y_0 = 50°$N. Note that for this cosine-shaped anomaly, the total width of the torque $\overline{G}_1$ is $2L$, but the scale on which the torque varies (the half-width) is L. In section 3 we showed that the compensation is sensitive to the wave forcing amplitude and now want to verify the analytic prediction that the compensation is sensitive to the meridional extent of the wave forcing.

We use the default configuration of our model, where only the NOGW is present, and consider the response to the steady analytic wave forcing $\overline{G}_1$. We vary A and L to keep the total torque (proportional to AL) constant, using the values $A = 2 \times 10^{-6}$ m s^{-2} and $L = 5°$ to set the overall amplitude. Then, L is varied from 2.5° to 25°. The open circles in Fig. 9 indicate the different A and L values that we explored, hoping to cross the boundary from stability to instability. All integrations were preformed over 20 000 days and compared against an unperturbed control integration of equivalent length. Figure 7a (see labels "$L = 2.5$," "$L = 5.0$," ..., "$L = 25.0$") show that the compensation systematically decreases with L, despite the fact that the total torque is held constant. Consistent with the scaling theory, the torque is largely compensated until the width exceeds approximately 15°. We were somewhat surprised that the extremely wide torques (which are quite weak) were still partially compensated. This may be because the wide torques push farther into the subtropics, where PV gradients are weak, as seen in Fig. 8.

Figure 7b shows the bootstrap kernel density estimation of the compensation for the different experiments. It shows that the larger the meridional extent of the kernel density is, the larger the uncertainty is. We found that uncertainly increases substantially in the cases with weak compensation; this necessitates the long 20 000-day integrations. For these cases, the torque was stable, but so weak that it was practically inconsequential in comparison to the resolved wave driving. The uncertainty is less in all other integrations shown in Fig. 7a, largely because the torques are stronger in these experiments.

5. Interactions between NOGW and resolved waves

We have extensively explored the effect of the OGWD, but have not yet discussed the impacts of the NOGWD. In the following we consider the impact of changing from the Rayleigh drag of the Polvani and Kushner (2002) model, which was envisioned as a crude NOGWD scheme, to the Alexander and Dunkerton (1999) scheme. Figure 10 illustrates the differences between integrations with the parameterized NOGWD and corresponding integrations

with the Rayleigh drag, where we define the "gravity wave perturbation" as the difference between the Rayleigh drag and the Alexander–Dunkerton NOGWD. Two cases are considered: one in which the polar vortex is comparatively weak (vortex lapse rate parameter $\gamma = 4\,\mathrm{K\,km^{-1}}$) and one in which the vortex is stronger ($\gamma = 6\,\mathrm{K\,km^{-1}}$). In the $\gamma = 4\,\mathrm{K\,km^{-1}}$ case, the overall change is about $0.1 \times 10^9\,\mathrm{kg\,s^{-1}}$ at 70 hPa, or about 5% of the total circulation at this height. Clearly, not all the NOGWD perturbation is compensated. Indeed, the compensation measure $C = 0.46 \pm 0.03$, suggesting that the NOGWD perturbation is only moderately compensated. Closer inspection of Fig. 10a, however, suggests that the overall response cannot be simply linked to change in the NOGWD. By itself, the change in $\overline{G}_{\mathrm{NOGW}}$ would create a lot of small-scale structure, which is largely canceled out by opposite-sign resolved wave driving perturbations. The total change exhibits a broad structure, consistent with the mean circulation, and maintains a stable PV gradient.

In the $\gamma = 6\,\mathrm{K\,km^{-1}}$ case, the change is larger than before—about 15% of the total circulation. This is an example of an almost noncompensating case: $C = 0.21 \pm 0.04$. In the Southern Hemisphere we can clearly see some compensation, but in the Northern Hemisphere the situation is quite complicated. There is still significant anticorrelation between the change in the EPFD and the NOGWD/Rayleigh drag, suggestive of compensation on small scales. The overall change in EPFD on the large scales, however, is to amplify the NOGWD perturbation, increasing the circulation. This suggests that a naive decomposition of the downward control response underestimates the importance of the NOGWD. The NOGW scheme weakens the polar vortex relative to the integration with Rayleigh friction, which in turn can increase the net resolved wave driving of the stratosphere (Gerber 2012). The nonlinearity of the response suggests the danger of linearly attributing the overall BDC to different forms of wave drivings, even when compensation is weak.

The difference in compensation between the OGWD and NOGWD is likely due to the difference in their meridional structure. The meridional scale of OGW wave drag is tied to variations in subgrid-scale topography and the surface winds, leading to sharp torques in the stratosphere that are likely to drive instability. The Alexander and Dunkerton (1999) NOGWD is meant to capture nonlocalized sources, convection, fronts, etc., and therefore generates a broader torque that is less likely to be compensated.

6. Summary and conclusions

A new idealized modeling framework was developed to study the interactions between resolved and parameterized waves in the stratosphere. Orographic and nonorographic gravity wave parameterization schemes were implemented in a GFDL dynamical core driven by otherwise idealized forcing. The new model preserves the key characteristics of the troposphere–stratosphere coupled system explored in previous idealized studies (e.g., Polvani and Kushner 2002; Gerber and Polvani 2009) but now includes physically based momentum-conserving gravity wave parameterizations.

Based on reduced-wavenumber models, Holton (1984) and McLandress and McFarlane (1993) suggested that there can be substantial interaction between parameterized wave drag and the resolved wave driving in the mesosphere. We extended this observation to the stratosphere by perturbing the orographic gravity wave scheme in our model and explore the implications of this interaction to downward control. If the OGW drag is increased or decreased in particular region, the resolved wave drag (or Eliassen–Palm flux divergence) responded to compensate for the change, so that there is little net change in the total wave driving. Thus a decomposition of the BDC into its wave-driven components may imply large changes in the role of parameterized and resolved waves, but the overall circulation is remarkably robust. We found that this compensation is fairly robust to changes in the boundary conditions and radiative equilibrium fields, and so is independent on the details of the parameterized or resolved wave driving.

We interpret the compensation process as a response of the resolved waves to maintain a "sensible," stable circulation. An analysis of downward control in the QG limit suggests that strong and/or narrow wave forcing is likely to drive an unstable circulation. The Rossby radius of deformation appears as a natural parameter in the stability analysis, and perturbations on scales L smaller than this are quite likely to go unstable, as the QG-PV scales with L^{-4} in this limit. In addition, we have found that in this limit, the instability criterion is proportional to the square of the wave forcing height scale; that is, the larger the height extent becomes, the more likely the flow will go unstable. We confirmed this intuition with a systematic study using the nonlinear model. Keeping the total wave forcing constant, we found that compensation increases with decreasing meridional scale.

An important question is whether compensation occurs in comprehensive GCMs. The scale of gravity wave drag perturbations is controlled by small-scale topography and the structure of surface winds, which tend to vary on much smaller scales relative to L_d of the stratosphere. Hence, we expect compensation to occur. There is indirect evidence in a recent study by McLandress et al. (2012) using the Canadian Middle Atmosphere Model (CMAM). They found a remarkable degree of

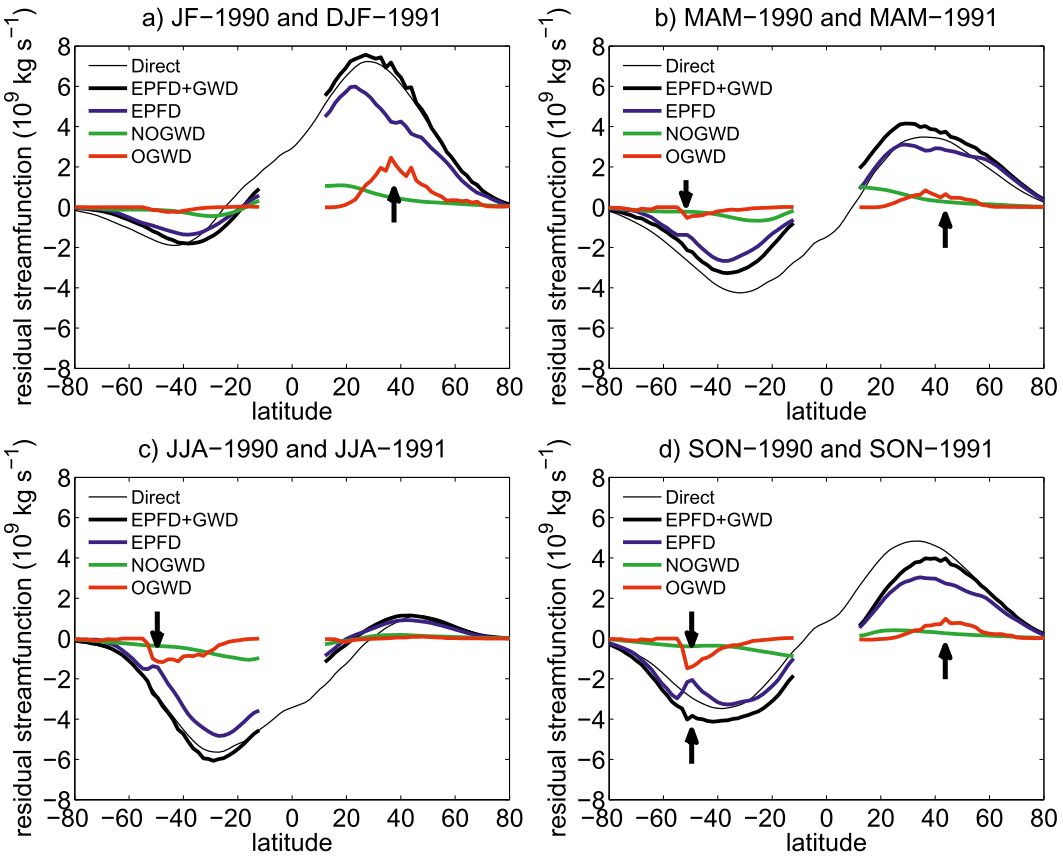

FIG. 11. Cross section of the residual mass meridional streamfunction at 70 hPa for the years 1990/91 using ECHAM6 data for the different seasons. The compensation "signature" is highlighted by a thick black arrow. Compare this figure to Figs. 6 and 10. As discussed in the text, the compensation signature is evident in the Southern Hemisphere, especially during (d) austral spring. The labels correspond to Fig. 6.

compensation to an OGWD perturbation located around 50° (see Figs. 11–15 in their paper), although this was not the focus of this study. There is also a hint of substantial interaction in climate change scenarios of CMAM as well (Shepherd and McLandress 2011). Compare their Fig. 2b to Fig. 5b of this paper: the negative correlation between the OGWD and the EPFD is the compensation signature.

The fact that compensation is more likely to occur for wave forcings of short meridional extent led us to suspect that it may be easier to find it in the Southern Hemisphere. Here the meridional structure of small-scale topography exhibits fine scales, particularly on the boundaries of the Southern Ocean with Patagonia and the Antarctic Peninsula. We obtained output from a comprehensive atmospheric GCM, ECHAM6, the atmosphere component of the MPI-ESM-MR model, developed at the Max Planck Institute for Meteorology (Stevens et al. 2012). Figure 11 shows cross sections of the residual streamfunction at 70 hPa for each season averaged over a 2-yr period. As expected, the winter and spring hemispheres show larger OGW activity. Compensation between the parameterized OGWD and the resolved waves is clearly evident in the negatively correlated peaks between the OGWD (red) and EPFD (blue) streamfunction, especially in the Southern Hemisphere. The forcing associated with GWD in ECHAM6 was generally on the order of 10^{-5} m s^{-2} and varies over regions 5°–10° wide, and so it is well into the nonlinear regime suggested by Fig. 9.

It is known that the current gravity wave parameterizations underestimate the temporal variability (or intermittency) of GW driving seen in observations (Geller et al. 2013). Parameterizations generally smooth out this intermittency, providing a more even torque in time. If actual gravity wave breaking events tend to involve very strong torques on short temporal scale, one might expect even more significant interaction with larger-scale waves through the instability mechanism explored in this text.

The strong interaction between resolved and parameterized waves has implications for both the modeling and the interpretation of the stratospheric circulation.

First, the total wave forcing in GCMs is often achieved by tuning the GWD to obtain a reasonable zonal-mean basic state (e.g., zonal wind, temperature)—a process that is typically not well documented but known to be a challenge. Compensation between resolved and parameterized waves implies that biases in the simulation of one component (i.e., the OGWD) can be masked by biases in other components. This makes it particularly difficult to identify and correct model biases. Getting the tuning right, however, is important: Sigmond and Scinocca (2010) found that subtle differences in the OGWD can have a significant impact on the tropospheric response to anthropogenic forcing.

A second implication is how we should interpret the driving of the Brewer–Dobson circulation. The BDC is often decomposed linearly into different wave-driven components using the downward control principle. The strong interaction between the resolved and parameterized wave driving indicates that this separation may provide an incomplete, or even misleading, illustration of the meridional circulation physics. This may explain the intermodel variance in the role of resolved and parameterized waves in driving the BDC. Models do tend to agree more on the total strength of the circulation than of individual components (e.g., Butchart et al. 2011, their Fig. 10). Compensation will tend to reduce the impact of difference in GW perturbation on the total circulation. This may also be relevant to analysis of future changes in the BDC, where GCMs agree on an increase in the circulation but disagree on the role of GW versus resolved waves.

To move forward, we recommend that modeling groups report more detailed information on the resolved and parameterized wave driving, which can be used to quantify the degree of compensation in their simulations. Monthly and zonal-mean EPFD and parameterized wave torques would be sufficient, allowing for the calculations shown in Fig. 11. There is also a need for observations (e.g., detailed measurements of temperature variance as a function of height) to better constrain the structure of GWD.

Even in cases with weak compensation as discussed in section 5, we still find a very nonlinear response of the resolved wave driving to changes in GWD, demonstrating that downward control is not additive. The idea that downward control is not linear in this sense puts some limitations on the controllability of a given forcing. In that context, downward control is limited by admissible stratospheric wave forcing, yet to be defined properly.

Acknowledgments. We thank Felix Bunzel and Hauke Schmidt at the Max Planck Institute for Meteorology for providing the ECHAM6 output. This research was supported in part by Grant AGS-0938325 from the National Science Foundation to New York University. We also thank Olivier M. Pauluis, Tiffany A. Shaw, M. Joan Alexander, and two anonymous reviewers for comments and suggestions.

APPENDIX

Gravity Wave Scheme Modifications

We specify the net momentum flux at the source level as a stress (Pa), as suggested by Alexander and Dunkerton (1999) and Donner et al. (2011). To the best of our knowledge, however, the net momentum flux at the source level in AM3's OGW parameterization appears to be interpreted as a flux ($m^2 s^{-2}$) with a tuning factor in order to get the correct Northern Hemisphere midlatitude stress. The AM3 settings were corrected by taking into account the density at the source level. This change does not have a significant impact on our integrations.

To avoid nonconservative wave driving, which can affect the stratosphere and troposphere downward control (Shepherd and Shaw 2004; Shaw and Shepherd 2007), we have added a simple condition to smoothly deposit all residual OGWD within the five layers above 0.5 hPa. Depositing it all in the uppermost level, as suggested by Shaw et al. (2009), led to instability, possibly because our model's top is substantially higher than that in their study. In the configuration of the scheme used in AM3, however, gravity wave flux above 30 hPa was allowed to escape to space. We also modified the NOGW parameterization to ensure that any residual flux was deposited in the uppermost level, although this had little impact on the integrations owing to the model's high top.

REFERENCES

Alexander, M. J., and T. J. Dunkerton, 1999: A spectral parameterization of mean-flow forcing due to breaking gravity waves. *J. Atmos. Sci.,* **56,** 4167–4182.

——, and Coauthors, 2010: Recent developments in gravity-wave effects in climate models and the global distribution of gravity-wave momentum flux from observations and models. *Quart. J. Roy. Meteor. Soc.,* **136,** 1103–1124.

Andrews, D. G., and M. E. McIntyre, 1978: Generalized Eliassen–Palm and Charney–Drazin theorems for waves in axisymmetric mean flows in compressible atmospheres. *J. Atmos. Sci.,* **35,** 175–185.

——, J. D. Mahlman, and R. W. Sinclair, 1983: Eliassen–Palm diagnostics of wave-mean flow interaction in the GFDL "SKYHI" general circulation model. *J. Atmos. Sci.,* **40,** 2768–2784.

Baldwin, M. P., and T. J. Dunkerton, 2001: Stratospheric harbingers of anomalous weather regimes. *Science,* **294,** 581–584.

Barenblatt, G., 1996: *Scaling, Self-Similarity, and Intermediate Asymptotics: Dimensional Analysis and Intermediate Asymptotics.* Cambridge Texts in Applied Mathematics, Vol. 14, Cambridge University Press, 412 pp.

Brewer, A. W., 1949: Evidence for a world circulation provided by the measurements of helium and water vapour distribution in the stratosphere. *Quart. J. Roy. Meteor. Soc.,* **75,** 351–363.

Bühler, O., 2009: *Waves and Mean Flows.* Cambridge University Press, 341 pp.

Butchart, N., and Coauthors, 2006: Simulations of anthropogenic change in the strength of the Brewer–Dobson circulation. *Climate Dyn.,* **27,** 727–741.

——, and Coauthors, 2010: Chemistry–climate model simulations of twenty-first century stratospheric climate and circulation changes. *J. Climate,* **23,** 5349–5374.

——, and Coauthors, 2011: Multimodel climate and variability of the stratosphere. *J. Geophys. Res.,* **116,** D05102, doi:10.1029/2010JD014995.

Charlton, A. J., and L. M. Polvani, 2007: A new look at stratospheric sudden warmings. Part I: Climatology and modeling benchmarks. *J. Climate,* **20,** 449–469.

Charney, J. G., and P. G. Drazin, 1961: Propagation of planetary-scale disturbances from the lower into the upper atmosphere. *J. Geophys. Res.,* **66,** 83–109.

Dobson, G. M. B., D. N. Harrison, and J. Lawrence, 1929: Measurements of the amount of ozone in the Earth's atmosphere and its relation to other geophysical conditions. Part III. *Proc. Roy. Soc. London,* **122A,** 456–486.

Donner, L. J., and Coauthors, 2011: The dynamical core, physical parameterizations, and basic simulation characteristics of the atmospheric component AM3 of the GFDL global coupled model CM3. *J. Climate,* **24,** 3484–3519.

Edmon, H. J., B. J. Hoskins, and M. E. McIntyre, 1980: Eliassen–Palm cross sections for the troposphere. *J. Atmos. Sci.,* **37,** 2600–2616.

Efron, B., and R. Tibshirani, 1994: *An Introduction to the Bootstrap*. Taylor & Francis, 456 pp.

Eyring, V., T. G. Shepherd, and D. W. Waugh, Eds., 2010: SPARC report on chemistry climate model validation. SPARC Rep. 5, WCRP-30, WMO/TD-40, 426 pp. [Available online at http://www.sparc-climate.org/publications/sparc-reports/sparc-report-no5/.]

Fritts, D. C., and M. J. Alexander, 2003: Gravity wave dynamics and effects in the middle atmosphere. *Rev. Geophys.,* **41,** 1003, doi:10.1029/2001RG000106.

Garcia, R. R., 1987: On the mean meridional circulation of the middle atmosphere. *J. Atmos. Sci.,* **44,** 3599–3609.

——, and W. J. Randel, 2008: Acceleration of the Brewer–Dobson circulation due to increases in greenhouse gases. *J. Atmos. Sci.,* **65,** 2731–2739.

Geller, M. A., and Coauthors, 2013: A comparison between gravity wave momentum fluxes in observations and climate models. *J. Climate,* **26,** 6383–6405.

Gerber, E. P., 2012: Stratospheric versus tropospheric control of the strength and structure of the Brewer–Dobson circulation. *J. Atmos. Sci.,* **69,** 2857–2877.

——, and L. M. Polvani, 2009: Stratosphere–troposphere coupling in a relatively simple AGCM: The importance of stratospheric variability. *J. Climate,* **22,** 1920–1933.

Haynes, P., 2005: Stratospheric dynamics. *Annu. Rev. Fluid Mech.,* **37,** 263–293.

——, M. E. McIntyre, T. G. Shepherd, C. J. Marks, and K. P. Shine, 1991: On the ''downward control'' of extratropical diabatic circulations by eddy-induced mean zonal forces. *J. Atmos. Sci.,* **48,** 651–678.

Held, I. M., and M. J. Suarez, 1994: A proposal for the intercomparison of the dynamical cores of atmospheric general circulation models. *Bull. Amer. Meteor. Soc.,* **75,** 1825–1830.

Holton, J. R., 1984: The generation of mesospheric planetary waves by zonally asymmetric gravity wave breaking. *J. Atmos. Sci.,* **41,** 3427–3430.

——, P. H. Haynes, M. E. McIntyre, A. R. Douglass, R. B. Rood, and L. Pfister, 1995: Stratosphere-troposphere exchange. *Rev. Geophys.,* **33,** 403–439.

Li, F., J. Austin, and J. Wilson, 2008: The strength of the Brewer–Dobson circulation in a changing climate: Coupled chemistry–climate model simulations. *J. Climate,* **21,** 40–57.

McLandress, C., and N. A. McFarlane, 1993: Interactions between orographic gravity wave drag and forced stationary planetary waves in the winter Northern Hemisphere middle atmosphere. *J. Atmos. Sci.,* **50,** 1966–1990.

——, and T. G. Shepherd, 2009: Simulated anthropogenic changes in the Brewer–Dobson circulation, including its extension to high latitudes. *J. Climate,* **22,** 1516–1540.

——, ——, S. Polavarapu, and S. R. Beagley, 2012: Is missing orographic gravity wave drag near 60°S the cause of the stratospheric zonal wind biases in chemistry climate models? *J. Atmos. Sci.,* **69,** 802–818.

Pierrehumbert, R. T., 1987: An essay on the parameterization of orographic gravity wave drag. *Proc. Seminar/Workshop on Observation, Theory and Modeling of Orographic Effects,* Reading, United Kingdom, ECMWF, Vol. 1, 251–282.

Polvani, L. M., and P. J. Kushner, 2002: Tropospheric response to stratospheric perturbations in a relatively simple general circulation model. *Geophys. Res. Lett.,* **29,** doi:10.1029/2001GL014284.

Shaw, T. A., and T. G. Shepherd, 2007: Angular momentum conservation and gravity wave drag parameterization: Implications for climate models. *J. Atmos. Sci.,* **64,** 190–203.

——, M. Sigmond, T. G. Shepherd, and J. F. Scinocca, 2009: Sensitivity of simulated climate to conservation of momentum in gravity wave drag parameterization. *J. Climate,* **22,** 2726–2742.

Shepherd, T. G., and T. A. Shaw, 2004: The angular momentum constraint on climate sensitivity and downward influence in the middle atmosphere. *J. Atmos. Sci.,* **61,** 2899–2908.

——, and C. McLandress, 2011: A robust mechanism for strengthening of the Brewer–Dobson circulation in response to climate change: Critical-layer control of subtropical wave breaking. *J. Atmos. Sci.,* **68,** 784–797.

Sigmond, M., and J. F. Scinocca, 2010: The influence of the basic state on the Northern Hemisphere circulation response to climate change. *J. Climate,* **23,** 1434–1446.

Solomon, S., K. H. Rosenlof, R. W. Portmann, J. S. Daniel, S. M. Davis, T. J. Sanford, and G.-K. Plattner, 2010: Contributions of stratospheric water vapor to decadal changes in the rate of global warming. *Science,* **327,** 1219–1223.

Son, S.-W., and Coauthors, 2010: Impact of stratospheric ozone on Southern Hemisphere circulation change: A multimodel assessment. *J. Geophys. Res.,* **115,** D00M07, doi:10.1029/2010JD014271.

Stern, W. F., and R. T. Pierrehumbert, 1988: The impact of an orographic gravity wave drag parameterization on extended-range predictions with a GCM. Preprints, *Eighth Conf. on Numerical Weather Prediction,* Baltimore, MD, Amer. Meteor. Soc., 745–750.

Stevens, B., and Coauthors, 2012: The atmospheric component of the MPI-M Earth System Model: ECHAM6. *J. Adv. Model. Earth Syst.,* **5,** 146–172, doi:10.1002/jame.20015.

Thompson, D. W. J., and S. Solomon, 2002: Interpretation of recent Southern Hemisphere climate change. *Science,* **296,** 895–899.

Vallis, G., 2006: *Atmospheric and Oceanic Fluid Dynamics: Fundamentals and Large-Scale Circulation.* Cambridge University Press, 772 pp.

Wilks, D. S., 1997: Resampling hypothesis tests for autocorrelated fields. *J. Climate,* **10,** 65–82.